J. Mech. Phys. Solids 151 (2021) 104378

Contents lists available at ScienceDirect

Journal of the Mechanics and Physics of Solids

journal homepage: www.elsevier.com/locate/jmps

Modeling peak-aged precipitate strengthening in Al–Mg–Si alloys

Yi Hu *, W.A. Curtin

Laboratory for Multiscale Mechanics Modeling (LAMMM), École Polytechnique Fédérale de Lausanne, 1015 Lausanne, Switzerland

ARTICLE INFO

Keywords:
Al–Mg–Si alloy
Peak aging
Precipitation strengthening
Orowan mechanism
Precipitate shear mechanism
Dislocation precipitate interaction
Discrete Dislocation Dynamics

ABSTRACT

Strengthening by needle-shaped β'' precipitates is critical in Al–Mg–Si alloys. Here, the strengthening is studied computationally at the peak-aged condition where precipitate shearing and Orowan looping are usually considered to have equal strengths. Pseudo-random precipitate microstructures are constructed based on experimental precipitate dimensions and volume fractions at peak aging. A Discrete Dislocation Dynamics method is then adapted to compute the Critical Resolved Shear Stress (CRSS) for Orowan looping of dislocations moving through the non-shearable precipitate field. The CRSS for Orowan looping is determined by a typical in-situ precipitate spacing that is smaller than the average spacing and by the dislocation core energy within a radius of ≈5b, a factor rarely considered. The matrix misfit stresses, volume fraction, and precipitate shape have small effects on the CRSS. With microstructure and property details introduced as faithfully as possible, the CRSS for Orowan looping using atomistically-calibrated core energies at room temperature is nonetheless ≈33% higher than experiments. This suggests that precipitate shearing controls strength, and analyses of (i) forces acting on the precipitates, (ii) misfit stresses inside the precipitates, (iii) first-principles results for the relevant precipitate fault energies, and (iv) simulations that mimic precipitate shearing indicate a shearing CRSS closer to experiments. Thus, Orowan looping only sets an upper bound for the CRSS even at peak aging, and further quantitative progress requires detailed modeling of precipitate shearing.

1. Introduction

Aluminum alloys are attractive structural metals due to their light weight, high strength, corrosion resistance, and ductility. In particular, the Al 6xxx (Al–Mg–Si) alloys are used extensively in automobiles while also finding other applications. The strength of Al–Mg–Si alloys is mainly attributed to precipitation strengthening. Alloy performance also varies with composition, and so the alloy design space is large and many different alloys have been studied carefully. Experimental studies probe the alloy strength as a function of processing conditions (aging time and temperature) to identify peak-aged conditions at which the strength is a maximum. The precipitation process in Al–Mg–Si under the T6 heat treatment sequence is (i) annealing at a high temperature to create a solid solution state, (ii) quenching to room temperature, (iii) heat treatment at about 180 °C for 2 h, and (iv) cooling to room temperature (Nie, 2014). If the aging treatment in step (iii) is shorter or longer, the material is under- or over-aged. The overall precipitation process from under-aged to over-aged condition is understood to be GP zones (clusters) → β'' → β' → β (Andersen et al., 2018). Peak strengthening is obtained when the β'' precipitates dominate in a fine-scale microstructure (Marioara et al., 2006, 2005).

Precipitate strengthening is understood theoretically in terms of two basic mechanisms (Nembach, 1997): (i) dislocation shearing of the precipitates and (ii) Orowan looping where the dislocations bow around the precipitates and leave Orowan loops. The

* Corresponding author.
E-mail address: yi.hu@epfl.ch (Y. Hu).

https://doi.org/10.1016/j.jmps.2021.104378
Received 29 October 2020; Received in revised form 13 February 2021; Accepted 17 February 2021
Available online 27 February 2021
0022-5096/© 2021 The Authors. Published by Elsevier Ltd. This is an open access article under the CC BY-NC-ND license (http://creativecommons.org/licenses/by-nc-nd/4.0/).

Critical Resolved Shear Stress (CRSS) is evaluated for both mechanisms and the smaller of the two is the operative CRSS for the system (Nembach, 1997). At a fixed volume fraction f, basic models predict that the CRSS for the Orowan process decreases with precipitate size r as $1/r$ while the CRSS for shearing increases as $\sqrt{r}$. Thus, there is an optimal precipitate size at which the two processes are equal and the strength is a maximum. Quantitatively, the strength should also depend on volume fraction, precipitate microstructure, misfit stresses caused by the lattice and elastic mismatch between coherent precipitates and the matrix, elastic mismatch effects on the dislocation motion, and any residual solute strengthening in the matrix. All of these processes are, in principle, thermally-activated (and thus temperature- and strain-rate-dependent). Therefore, all these effects need to be considered carefully in any attempt to understand or model experiments.

Because of its technological importance, the key phases in Al–Mg–Si alloys are well-studied (Andersen et al., 1998) including composition dependence (Marioara et al., 2005) and the effects of processing on the precipitate microstructure (Wenner et al., 2012). Complementary simulation studies have computed precipitate properties and precipitates embedded in the Al matrix using first-principles methods (Ninive et al., 2014; Giofré et al., 2017). Without accurate interatomic potentials (but see Kobayashi et al., 2017 and Jain et al., 2021), atomistic simulations of dislocation/precipitate interactions in Al–Mg–Si alloys have not been reported, although similar studies exist using approximate potentials for Al–Cu (Singh and Warner, 2013) and Mg–Al alloys (Esteban-Manzanares et al., 2019; Vaid et al., 2019). It has been more common to use mesoscale Discrete Dislocation Dynamics (DDD) to examine Orowan looping, but usually focused on idealized microstructures with spherical (Mohles and Nembach, 2001; Monnet et al., 2011) or ellipsoidal inclusions (Aagesen et al., 2018), often without misfit stresses or elastic mismatch effects. In parallel, analytical models based on basic mechanisms have been used to fit the strength of Al–Mg–Si alloys (Myhr et al., 2018; Bardel et al., 2014) but involve empirical parameters that limit predictive capability.

The general issues for computations in Al–Mg–Si are (1) can the peak-aged strength be predicted accurately without fitting and (2) if so, can computations provide some guidance for alloy development? Here, we address the first question using state-of-the-art methods. Specifically, we take advantage of the peak aging condition and study the Orowan mechanism in realistic peak-aged microstructures of β'' precipitates. We incorporate accurate misfit strains, neglect the (small) elastic mismatch effects, and neglect solute strengthening since nearly all the Mg and Si additions are in the precipitates. We find that misfit stress effects on Orowan looping are small but that the dislocation core energy is very important for quantitative results. With atomistically-calibrated core energies, which are much lower than the default core energy in the widely used DDD code `ParaDiS`, we find that the CRSS for Orowan looping is ≈50% above experiments using T = 0 K core energies and 33% above experiments using a T = 300 K core energy. This suggests that precipitate shearing at a lower CRSS controls the peak-aged strength. A preliminary analysis of shearing is made and the estimated CRSS is in better agreement with experiments, motivating future work on detailed modeling of precipitate shearing even at peak-aging.

We conclude that quantitative simulations of the CRSS in alloys with nanoscale precipitate microstructures require accurate (i) statistical microstructures, (ii) dislocation core energies (with long-range elastic effects being negligible), (iii) precipitate fault energies, and (iv) internal precipitate misfit stresses. Incorporating the first two using DDD simulations provides a "best" upper-limit to the CRSS via the Orowan mechanism but also shows that shearing and accurate internal misfit stresses cannot be neglected; this requires further analysis and extensions of DDD simulations to incorporate shearing. The case study here on Al–Mg–Si provides a clear framework for connecting precipitate microstructures and fault energies to macroscopic strength, which can aid in guiding experimental development and assessment of new alloys.

The current paper is organized as follows. In Section 2, we describe our method for creating realistic pseudo-random precipitate microstructures for peak-aged Al–Mg–Si. Section 3 presents the calculation of the misfit stresses in these microstructures. In Section 4, we discuss the design and execution of mescoscale simulation of dislocation motion through the precipitate microstructures using Discrete Dislocation Dynamics simulations. Section 5 presents simulation results, analysis of the features controlling the strengthening, and comparisons with experiments. Section 6 presents initial analyses of the shearing mechanism and the associated CRSS. The final section summarizes our main findings.

2. Pseudo-random precipitate microstructures of peak-aged Al–Mg–Si

Existing TEM studies reveal that the β'' precipitates have a monoclinic crystal structure (Andersen et al., 1998). They form as needle-like precipitates aligned with the fcc Al cubic axes, with the orientation relationship

$$\mathbf{a} = [100]_{\beta''} \parallel [203]_{\mathrm{Al}}, \quad \mathbf{b} = [010]_{\beta''} \parallel [010]_{\mathrm{Al}}, \quad \mathbf{c} = [001]_{\beta''} \parallel [\bar{3}01]_{\mathrm{Al}}$$

There are three possible precipitate orientations corresponding to the precipitate **b** aligned along the matrix [100], [010], and [001] directions, respectively. There are also three main precipitate compositions (Mg_5Si_6, $Mg_5Al_2Si_4$, $Mg_4Al_3Si_4$) with slightly different crystal dimensions and elastic constants; these differences are negligible within the study performed here. Experiments at peak aging (Wenner et al., 2012) provide information on the precipitate dimensions (cross-sectional area A and length l) and volume fraction f. Table 1 shows relevant experimental data on the precipitates and microstructures. The precipitates form by a process of nucleation and growth, as solutes in the matrix diffuse to the precipitates, and then grow further by Ostwald ripening. This formation process suggests that the microstructure is not random but instead has precipitate spacings that are more narrowly distributed around the mean value. These considerations motivate our creation of pseudo-random microstructures as follows.

Our initial building block for a realistic microstructure is a cubic cell based on the experimental precipitate dimensions and volume fraction. Three precipitates, one for each orientation, are placed in a cubic cell such that periodic replication of the cell in all three cubic directions gives equal spacings among all precipitates and their periodic images. At precipitate volume fraction f

Table 1
List of experimental characterization of β'' phases in Wenner et al. (2012) and Maisonnette et al. (2011), and the corresponding simulated precipitate dimensions and building block sizes. The length for each lattice vector of precipitate is from Mg_5Si_6 for reference.

f	Precipitate type	Experiment		Simulated precipitate in lattice unit			l_c (nm)
		A (nm^2)	l (nm)	**a** $[203]_{Al}$ (15.14 Å)	**b** $[010]_{Al}$ (4.08 Å)	**c** $[\bar{3}01]_{Al}$ (6.93 Å)	
0.66%	Mg_5Si_6	7.5	22.5	2	55	4	41.9
1.10%	$Mg_4Al_3Si_4$	8.1	37.8	3	93	3	43.8
1.10%	$Mg_4Al_3Si_4$	8.1	37.8	2	93	4	42.1
1.60%	Mg_5Si_6	21.2	25	3	61	8	46.5

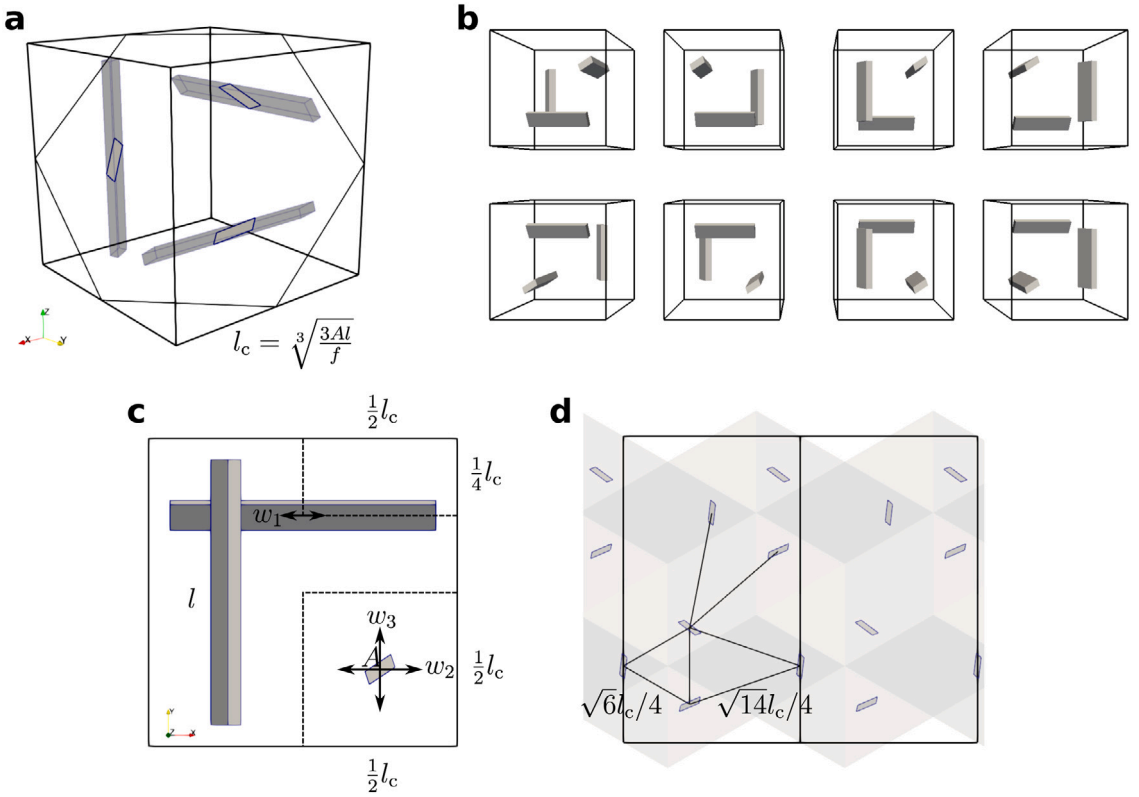

Fig. 1. (a) Building block of the micro(100) pseudo-random structure with three equi-spaced precipitates aligned in three axis directions, with A the precipitate cross sectional area, l the precipitate length, and l_c the edge length of the cubic cell. (b) The 8 equivalent variants of the fundamental building block. (c) In-plane projection of the building block for micro(100) showing the range of random perturbations w_1, w_2 and w_3 added to each precipitate position. (d) Precipitate structure of an ideal single-variant unperturbed micro(100) structure on a (111) slip plane, showing two different precipitate spacings.

and number of density ρ (Wenner et al., 2012), the edge length of the cubic cell is $l_c = \sqrt[3]{3Al/f}$ or $l_c = \sqrt[3]{3/\rho}$. There are 8 variants of this fundamental building block, as shown in Fig. 1(b), created by rotations and/or reflections of the basic cell.

Pseudo-random microstructures labeled as micro(100) are then created as 3 × 3 × 3 assemblies containing 27 of the initial building blocks with variants randomly chosen from the 8 possibilities shown in Fig. 1(b). Further, we perturb the center position of each precipitate in each building block in the [100], [010] and [001] directions as indicated by the w_i and their ranges shown in Fig. 1(c). These perturbations are limited only by the restrictions that each precipitate remains in its original cubic cell and that the precipitates do not overlap. In an infinite non-periodic microstructure, the average precipitate area fraction on (111) slip planes is exactly equal to the volume fraction f. The perturbations imposed here generate microstructures having precipitate area fractions on the (111) slip planes very near f (e.g. between 1.0% and 1.2% for a microstructure with average f = 1.10%. Furthermore, for simulations below, we then study slip only on (111) planes having the correct average precipitate area fraction.

Fig. 2 shows one example of a pseudo-random microstructure created in this manner, corresponding to the volume fraction and dimensions from experiment (Wenner et al., 2012) with a micrograph from the experiment also shown. The visual correspondence is good. However, when the precipitates are not permitted to extend outside the individual building block, there are regions of zero precipitate along the building block boundaries. These create similar regions on the (111) slip planes of the microstructure. Fig. 1(d) further shows that the equal spacing of the periodic precipitates in the cubic directions leads to two different length scales on the (111) planes where the dislocations glide. This might affect dislocation behavior as well.

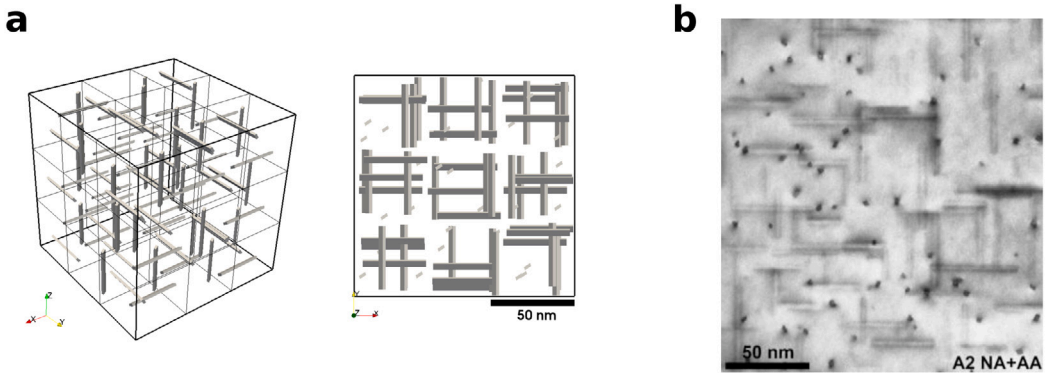

Fig. 2. (a) 3 × 3 × 3 pseudo-random precipitate model with micro(100) corresponding to the alloy denoted A2 (NA+AA) in Wenner et al. (2012). (b) Corresponding experimental micrograph in Wenner et al. (2012). The scale bars in (a) and (b) are the same.

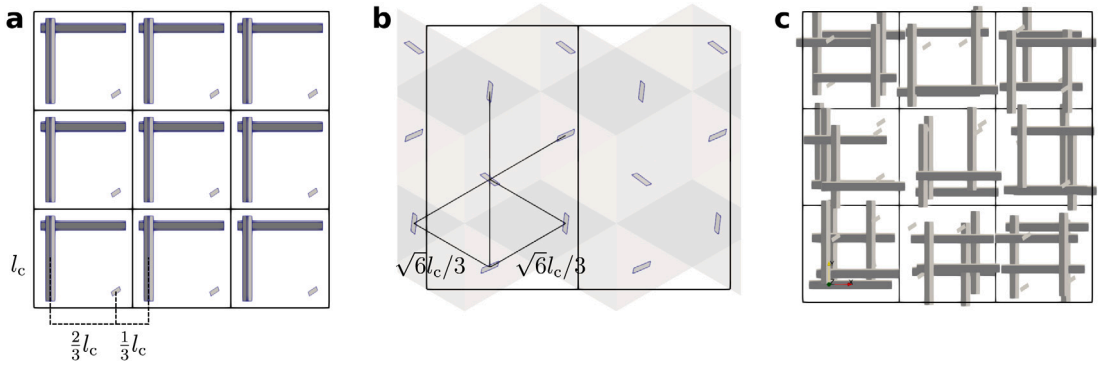

Fig. 3. (a) Precipitate structure of an ideal single-variant unperturbed micro(111) showing two different precipitate spacings in the (100) projection. (b) The same microstructure but on the (111) plane, showing equal precipitate spacing on the (111) plane. (c) Projection of a full 3 × 3 × 3 micro(111) microstructure generated with large perturbations of the individual precipitates.

To rectify possible issues with the above micro(100) structures, we have created a second family of microstructures denoted as micro(111). As shown in Fig. 3, the precipitate spacings in the cubic direction of micro(111) are unequal but the precipitate spacings on the (111) planes are equal. Furthermore, we consider perturbations in which the precipitates can extend outside of their individual blocks, eliminating the precipitate-free regions along the block boundaries (Fig. 3(c)). The micro(111) structures again have nearly-average precipitate area fractions on all (111) planes, and simulations are performed on (111) planes very near the average area fraction.

Finally, while we report below only small sample-to-sample variations in the strength at size 3 × 3 × 3, indicating sufficient sampling, we also created several micro(100) structures of size 5 × 5 × 5 to examine convergence. We also studied several microstructures with random placement of precipitate cross-sections on the (111) plane.

Using the above general procedure, specific microstructures based on experimental studies were created as shown in Table 1. The primary microstructure has $f = 1.10\%$ with $Mg_4Al_3Si_4$ precipitates corresponding to the alloy denoted A2(NA+AA) in Ref. Wenner et al. (2012). For the low Mg concentration (0.443 at.%) in this alloy, $Mg_4Al_3Si_4$ is the only possible composition at $f = 1.10\%$ and the residual solute concentration are $c_{Mg}^{sol} = c_{Mg} - 4f/11 = 0.043$ at.% and $c_{Si}^{sol} = 0.402$ at.% so that residual solute strengthening is negligible. For this system, we consider two different precipitate shapes ($2\mathbf{a} \times 4\mathbf{c}$ and $3\mathbf{a} \times 3\mathbf{c}$) having similar cross-sectional area but different shape. To evaluate the effect of volume fraction, we created microstructures with $f = 0.66\%$ and $f = 1.60\%$ using the properties of Mg_5Si_6. The first case is similar to the A3 alloy (particularly, A3_36h_175 °C) in Marioara et al. (2007) but with a slightly larger cross sectional area. The second case is similar to the alloy in Ref. Maisonnette et al. (2011) with a shorter length and larger cross-section area. While we use different precipitate compositions for different cases, the differences among them are negligible for our determination of the CRSS for Orowan looping.

3. Misfit stresses in the pseudo-random microstructures

The nanoscale β'' precipitates remain coherent with the Al matrix. The mismatch in size and shape of the precipitates relative to the closest corresponding region of Al atoms leads to the creation of misfit stresses in the matrix and the precipitates. This is observed in both previous experiments and DFT calculations (Wenner and Holmestad, 2016). It is thus necessary to determine the

Table 2
Elastic constants obtained by first principle calculation in Giofré et al. (2017). These elastic constants are used in eigenstress calculation.

[GPa]	C_{11}	C_{22}	C_{33}	C_{44}	C_{55}	C_{66}
Al		106.1			31.9	
Mg_5Si_6	98.4	84.6	88.0	21.9	29.1	51.2
$Mg_5Al_2Si_4$	107.1	94.7	99.1	26.9	36.3	49.4
$Mg_4Al_3Si_4$	106.7	96.5	97.1	25.9	35.6	46.3

C_{12}	C_{13}	C_{23}	C_{15}	C_{25}	C_{35}	C_{46}
	55.9			0.		
50.0	47.7	45.7	8.2	5.8	5.4	−10.1
40.3	45.6	43.0	−13.1	4.3	11.9	5.4
46.5	48.0	48.8	9.3	5.7	9.3	6.3

misfit strains throughout the microstructure and then incorporate those misfit stresses into simulations of dislocation motion through the microstructure.

The misfit stress field $\boldsymbol{\sigma}$ throughout a specified microstructure is calculated using a fast-fourier transform (FFT) method as follows. First, the precipitate misfit strain $\bar{\varepsilon}$ is computed relative to the underlying Al lattice. In general, the precipitate lattice vectors $\mathbf{a}_p$ are related to the matrix lattice vectors $\mathbf{a}_m$ by $\mathbf{a}_m = \bar{\mathbf{F}}\mathbf{a}_p$, where $\bar{\mathbf{F}}$ is the transformation deformation gradient. The precipitate misfit strain is then $\bar{\varepsilon} = \frac{1}{2}[\bar{\mathbf{F}}^T + \bar{\mathbf{F}}] - \mathbf{I}$. The linear-elastic stress–strain relationships for the matrix and precipitates are

$$\begin{cases} \boldsymbol{\sigma} = \mathbf{C}_m\boldsymbol{\varepsilon} & \text{in } \Omega_m \\ \boldsymbol{\sigma} = \mathbf{C}_p(\boldsymbol{\varepsilon} - \bar{\varepsilon}) & \text{in } \Omega_p \end{cases} \tag{1}$$

where $\mathbf{C}_p$ and $\mathbf{C}_m$ are the elastic constants of the precipitates and the Al matrix, respectively. We use the first-principles-computed values of Giofré et al. (2017) as shown in Table 2. The misfit stresses are obtained by solving the equilibrium equation $\nabla \cdot \boldsymbol{\sigma} = \mathbf{0}$ within the entire periodic pseudo-random microstructural simulation cell.

Taking advantage of the periodicity, we use a new fast-fourier transform (FFT) spectral solver (Junge et al., 2020) (see the Appendix) that discretizes the full structure into N pixels with each pixel assigned the appropriate elastic constants. The discrete FFT stress field has oscillations at the scale of the pixels. These are first reduced in size scale by using a fairly high resolution of $N = 301$ corresponding to a pixel size of 2.3b where b = 2.851 Å is the Al Burgers vector. We then apply a smoothing filter to reduce the remaining oscillations to a level that should have no effect on subsequent dislocation simulations.

The misfit stresses create Peach–Koehler forces $\mathbf{F} = (\boldsymbol{\sigma}\mathbf{b})\times\mathbf{t}$ acting on a dislocation with line direction $\mathbf{t}$. Glide of dislocations with Burgers vector $\mathbf{b} = [\bar{1}10]\ a/2$ on the (111) plane with normal vector $\mathbf{n}$ leads to a Peach–Koehler glide force $\mathbf{F}_g = (\mathbf{n}\cdot(\boldsymbol{\sigma}\mathbf{b}))(\mathbf{n}\times\mathbf{t})$. Thus, we compute the resolved shear stress (RSS) field $\mathbf{n}\cdot(\boldsymbol{\sigma}\,\mathbf{b})/|\mathbf{b}|$ that exerts forces in the glide plane acting normal to the dislocation line direction. Examples of the RSS field are presented in Fig. 4 for several microstructures. The RSS values in the matrix can be large – reaching +/− 600 MPa – but only very locally around the precipitates. Each precipitate has little interaction with other precipitates, and so all precipitates with the same orientation have nearly the same RSS. The sign of the RSS depends on the chosen $\mathbf{n}$ and $\mathbf{b}$, which are a matter of convention and are shown in each figure. These features will rationalize our conclusion that the role of misfit stresses on Orowan strengthening is quite small.

Inside the precipitates, the magnitude and sign vary significantly with both orientation and shape, as seen in detailed views in Fig. 4. These fields, while not important for Orowan looping, can thus assist or impede precipitate shearing as discussed in Section 6. Experimental measurements show large internal strains in the precipitates (Wenner and Holmestad, 2016), consistent with our results.

4. DDD simulations of dislocation-precipitate interactions

The motion of a dislocation through the precipitate field of the pseudo-random microstructures is modeling using the non-singular theory (Cai et al., 2006) for Discrete Dislocation Dynamics (DDD) as implemented in the open-source code `ParaDiS` (Arsenlis et al., 2007). Generically, DDD methods discretize continuum dislocation lines into linear segments, compute the long-range elastic interactions among all segments, and evolve the discretized dislocations according to the total driving force on each segment. The total driving force includes contributions from (i) an applied stress, (ii) the elastic interactions among segments, (iii) the self forces due to elasticity and dislocation core energy of individual segments, (iv) the image forces due to interactions with elastically-mismatched precipitates (Hirth and Lothe, 1982), and (v) the misfit stresses (RSS) created by the combination of lattice and elastic mismatch of the precipitates. Implementation requires careful attention to a range of details, as discussed below.

For a DDD simulation in `ParaDiS`, we first select a (111) glide plane from the 3d microstructure. Noting that the microstructure periodicity is different on a (111) plane, we replicate the full 3d precipitate microstructure to obtain a periodic microstructure on the chosen (111) plane, as indicated in Fig. 5(a). `ParaDiS` simulations are then performed within some even-larger periodic cubic cell. We insert our periodic (111) glide plane microstructure into such a cubic cell with the glide plane and desired dislocation line direction aligned with the cubic axes of the `ParaDiS` cell. A single dislocation is then introduced along the desired line direction, and sufficient periodic images along the line direction are added. Note that the absence of precipitate microstructure outside the actual (111) domain along the dislocation glide direction is unimportant. This outer region is simply a large surrounding elastic

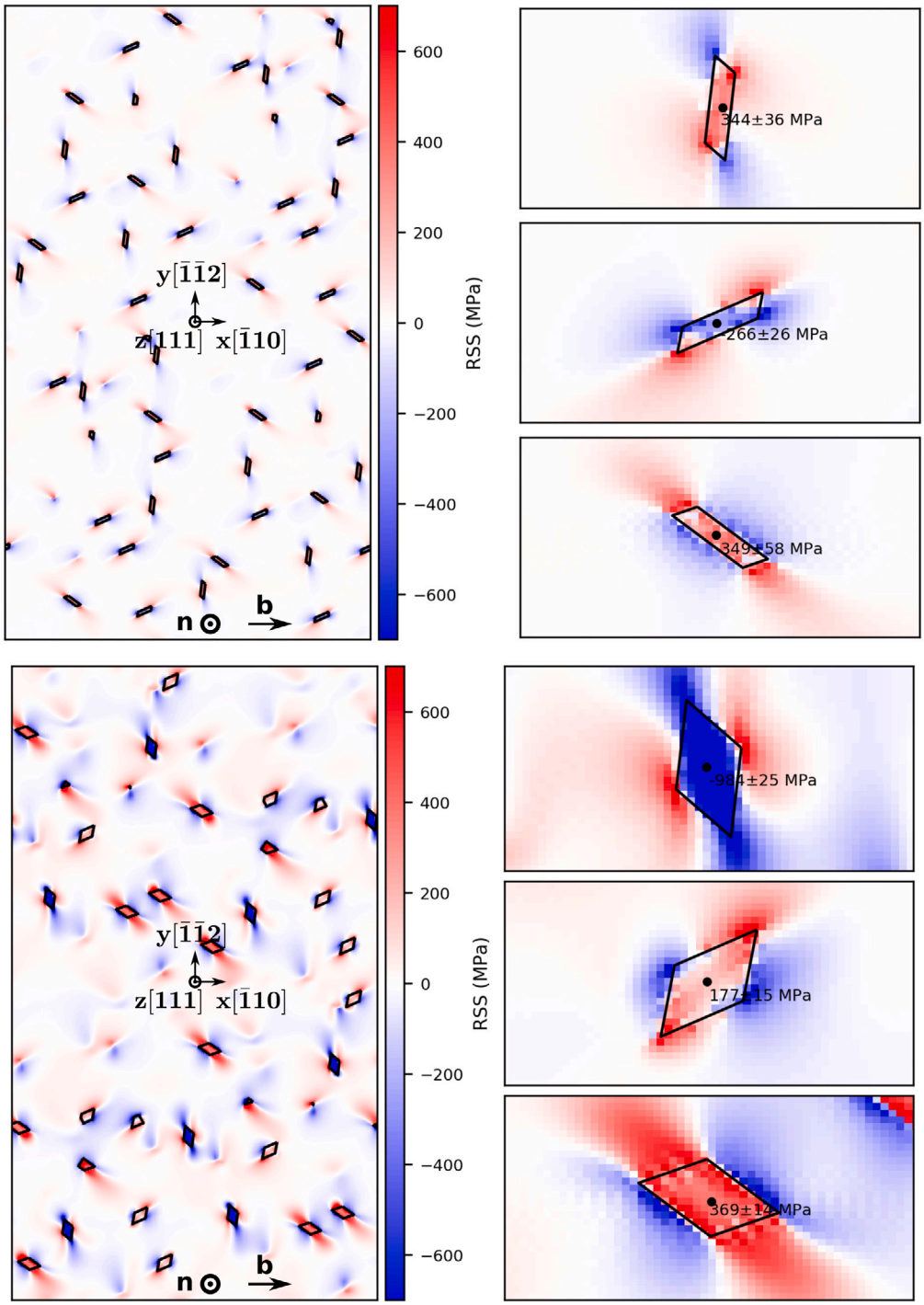

Fig. 4. Normalized Resolved Shear Stresses (RSS) due to precipitate misfit strains acting on a screw dislocation, as computed for two different microstructures (precipitate dimensions $3\mathbf{a}\times 3\mathbf{c}$ at $f = 1.10\%$, and $3\mathbf{a}\times 8\mathbf{c}$ at $f = 1.60\%$). The RSS are large very near the precipitates but decay rapidly with distance, as expected. The sign of the RSS varies with precipitate orientation, dislocation type, and chosen (111) slip plane. The average and standard deviation of the RSS inside the different precipitates are indicated, and play a role in precipitate shearing.

domain that prevents undesired image effects in ParaDiS while having no effect at all on the motion of the dislocation through the microstructured region. Examples of the (111) plane models within the larger ParaDiS cell, for both screw and edge dislocations,

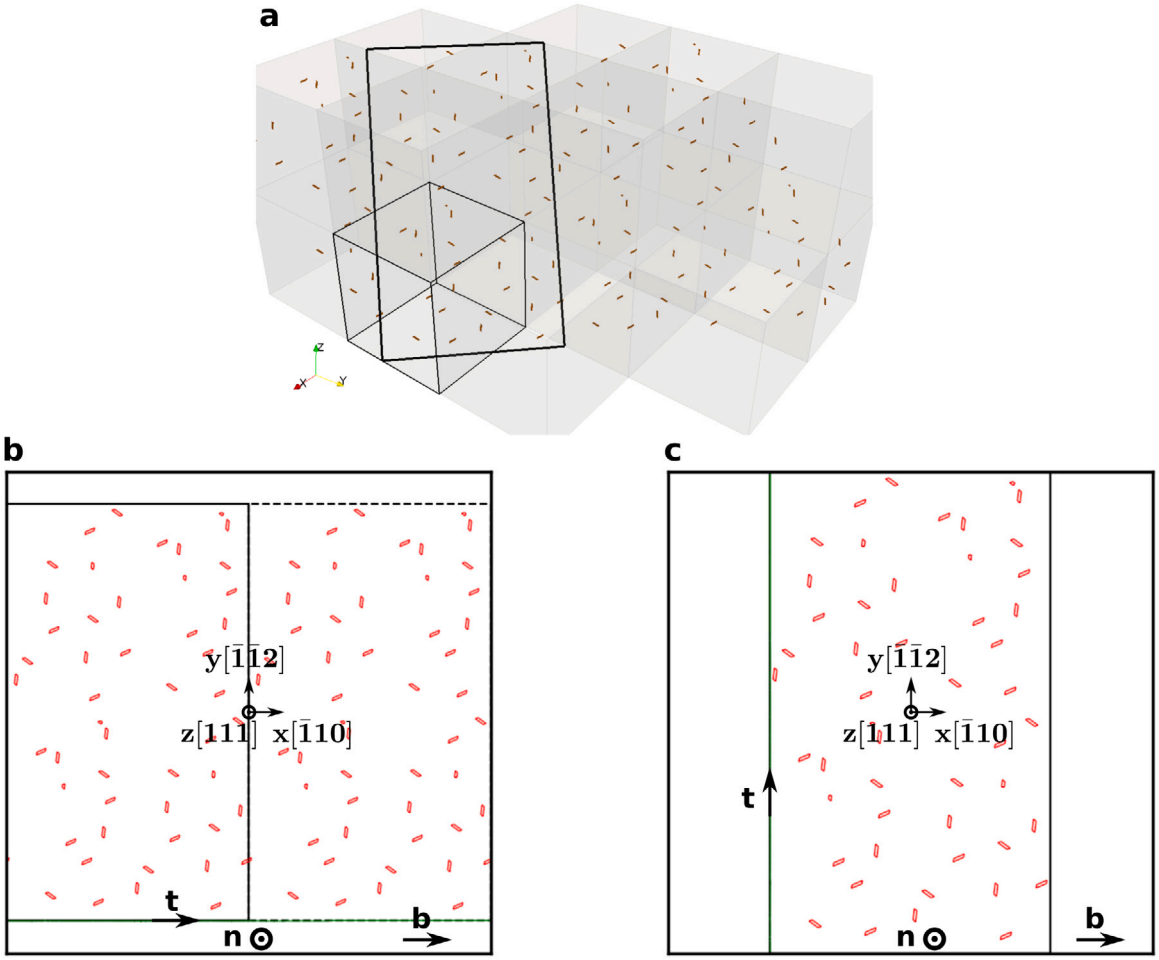

Fig. 5. (a) Periodicity of a (111) simulation plane as created from replication of an underlying $3\times3\times3$ microstructure, with precipitates intersecting the chosen glide plane shown. (b) Microstructure on the (111) plane for a DDD simulation for screw dislocation. The Burgers vector, line direction, and initial straight screw dislocation are shown. Red polygons show the boundaries of the cut precipitates in this glide plane. (c) as in (b) but for an edge dislocation.

are shown in Fig. 5(b) and (c). With periodic boundary conditions imposed in all directions within ParaDiS, we verify that the image forces on an infinite straight dislocation line are less than 3 MPa for the ParaDiS cell dimensions of over 1200b used here.

With a primary focus on Orowan looping on the glide plane, we treat the precipitates as impenetrable obstacles. Because the elastic moduli of the precipitates are generally close to those of the Al matrix, and because the cost of computing image forces due to the difference in elastic moduli is extremely high (Fivel, 2008), we neglect this effect. Then, the effect of the precipitates is entirely constrained to the glide plane of the dislocation. A precipitate is a region where the dislocation cannot be present while creating a spatially-varying misfit RSS outside the precipitate. We represent the precipitates by using prismatic loops along the exact boundary of the precipitates in the glide plane. The stress field created by a prismatic loop in the glide plane of the dislocation generates exactly zero driving force for the mobile dislocation on the same glide plane. Nonetheless, we explicitly set the forces to zero in ParaDiS by labeling nodes of the prismatic loops as "precipitate" and setting any interaction forces involving "precipitate" nodes to zero. The prismatic loop is thus fully fixed during the simulation. As a discretized lattice dislocation approaches a discretized prismatic loop (a precipitate), any node that comes within a pre-defined collision distance of 0.2b of the precipitate loop is assigned essentially zero velocity. The lattice dislocation thus conforms to the precise shape of the precipitate as it attempts to glide around it, with no spurious interactions and no numerical instabilities (see Fig. 6).

Most previous modeling of precipitates imposes some high artificial stress on the dislocations in the region occupied by precipitates (Queyreau and Devincre, 2009; Fivel, 2008; Mohles and Nembach, 2001; Lehtinen et al., 2016). This avoids the need to determine when the dislocation reaches the precipitate boundary. However, as mentioned in Mohles and Nembach (2001), this method can cause numerical problems at the precipitate boundary. Aagesen et al. (2018) use the exact geometry with dislocation nodes pinned at the precipitate interface, most similar to our approach. Work by Al-Cu (Santos-Güemes et al., 2018, 2020) used a very different method wherein the precipitate is fully modeled and the entire glide dislocation loop is represented by a discretized eigenstrain, enabling a full 3d FFT model. However, this treatment of the dislocation is more approximate and we prefer to use

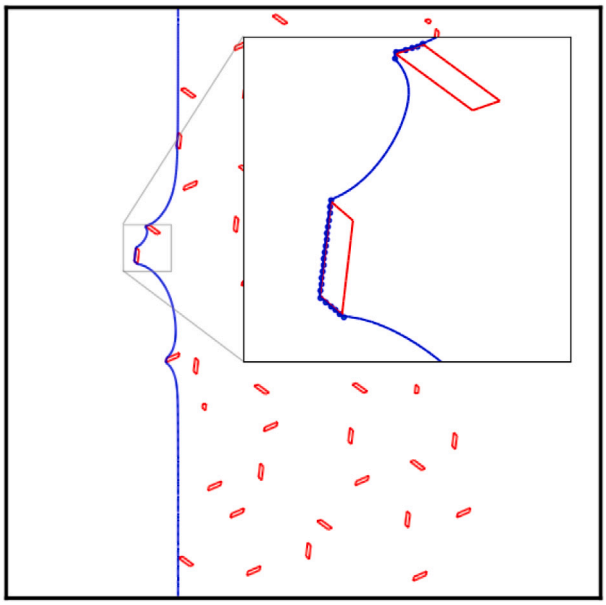

Fig. 6. Snapshot of the discretized dislocation interactions with precipitates in the DDD simulation. Dislocation nodes are pinned when they are within a distance 0.2b of the prismatic segments that define the precipitate. The nodes shown in the inset are those pinned at the precipitate in this configuration.

actual dislocation lines gliding in a 2d plane, with variable resolution and with control of the dislocation core energy, at the cost of neglecting the small dislocation/precipitate image interactions.

In addition to treatment of the dislocation-precipitate interactions, the simulations require material parameters such as the Burgers vector, elastic constants, dislocation core energy, non-singular regularization parameter "a", and dislocation mobility. We are examining only stable quasistatic solutions and so the mobility parameter is not important aside from being small enough to ensure numerical stability; we use the small value of 0.05b/s. `ParaDiS` performs automatic re-meshing and refinements of the time steps. The baseline elastic properties are taken from an EAM potential for Al (Ercolessi and Adams, 1994) with Bacon–Scattergood effective isotropic material moduli (Scattergood and Bacon, 1975) $\mu = 32.0$ GPa, $\nu = 0.34$.

The term core energy is imprecise. A dislocation only has a total self-energy but it is convenient to conceptually partition that energy into an "elastic" contribution and an "inelastic" or core contribution at the arbitrary but convenient reference length b as Hu et al. (2019), for dislocation character θ,

$$E(\theta) = K(\theta)\ln\left(\frac{R}{b}\right) + E_c(\theta)\big|_b \tag{2}$$

where $K(\theta)$ is an elastic parameter; for an isotropic material, $K(\theta) = \frac{\mu b^2}{4\pi}(\cos^2\theta + \frac{1}{1-\nu}\sin^2\theta)$. The above total energy can also be determined at any other reference length a as

$$E(\theta) = K(\theta)\ln\left(\frac{R}{a}\right) + K(\theta)\ln\left(\frac{a}{b}\right) + E_c(\theta)\big|_b \tag{3a}$$

$$= K(\theta)\ln\left(\frac{R}{a}\right) + E_c(\theta)\big|_a \tag{3b}$$

thereby defining a core energy quantity at scale a. In non-singular dislocation theory, a is the non-singular regularization parameter. To calibrate non-singular theory to an atomistic calculation of the total energy within a radius $R \gg a$ requires subtracting an additional constant self-energy term that appears in non-singular theory and then adding an energy such that the total energy within radius $R \gg a$ exactly matches the atomistic total energy (Hu et al., 2019) . The total self-energy is then independent of the choice of regularization parameter a. Nonetheless, comparisons of `ParaDiS` and atomistic simulations of dislocation bow-out show that some values of a are slightly better than others. Here, we use the calibration of Hu et al. (2019) to atomistic Al as described by the Ercollessi–Adams EAM potential, for which $a = 5.4b$ was found optimal; other calibrations are considered in Section 5.3.

We load the system with a resolved shear stress τ on the glide plane to move screw dislocations in the positive y direction and edge dislocations in the positive x direction. The critical resolved shear stress (CRSS) for Orowan looping is obtained by incrementing the applied stress. If the change in maximum advance of the dislocation in the glide direction is less than 0.1b for 300 time steps, we increment the load by 5 MPa. When a stress increment exceeds the CRSS, the dislocation moves forward through the remaining sections of the microstructure. The CRSS τ_c is then in between two load increments differing by 5 MPa, and is quoted as the mean value with an uncertainty of $\tau_c \pm 2.5$ MPa. Fig. 7 shows examples of the edge and screw dislocations just below and just above τ_c in one typical microstructure.

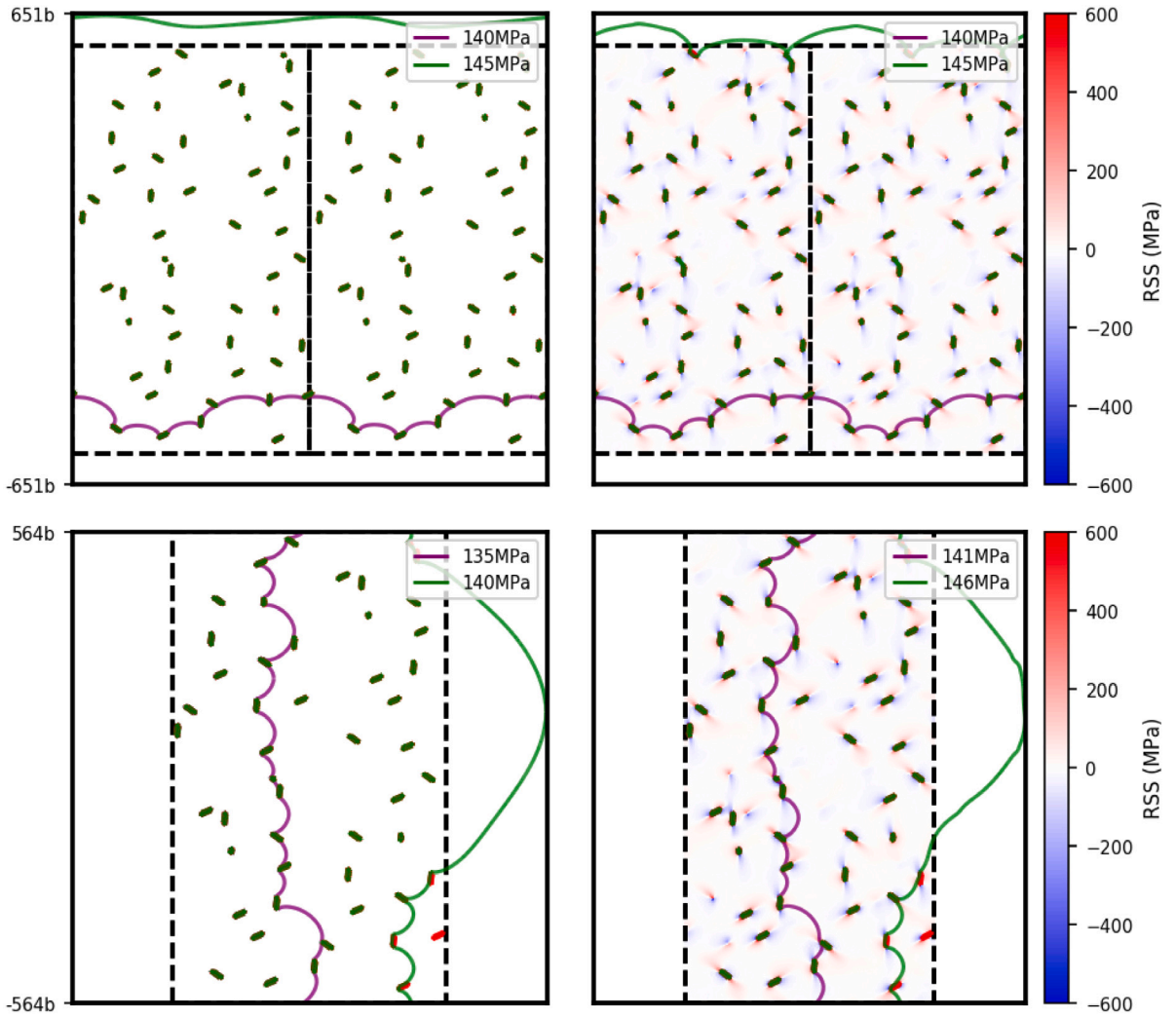

Fig. 7. DDD configurations for screw (top) and edge (bottom) simulations at stresses just before and just after Orowan looping for one particular $f = 1.10\%$ microstructure and glide plane, and for simulations with and without misfit stresses. The misfit stresses have minimal effect on the critical dislocation configuration.

5. CRSS for Orowan looping

5.1. CRSS versus volume fraction and misfit stress

Simulations of Orowan looping in our realistic micro(100) microstructures were performed at volume fractions 0.66%, 1.10% and 1.60% using $\mu = 32.0$ GPa, $\nu = 0.34$ and the Ercolessi–Adams core energy at cut-off $5.4b$ (Hu et al., 2019). For each volume fraction, two micro(100) pseudo-random structures were created (Section 2) using precipitate dimensions in Table 1. In particular, we use a more-rectangular cross section $3\mathbf{a} \times 3\mathbf{c}$ for $f = 1.10\%$ to mimic experiments (see Fig. 4 in Wenner et al., 2012) while for volume fractions $f = 0.66\%$ and $f = 1.10\%$ we use an equiaxed more-diamond-like shape; we address any shape effects subsequently. Four different (111) glide planes were studied for each microstructure. The averaged CRSS values for edge and screw dislocations over all simulations are shown in Table 3 along with the standard deviations.

Comparing the screw and edge simulations, the CRSS for the screw dislocation is only slightly higher (20 MPa) than the CRSS for the edge dislocation across all cases. A much higher strength for the screw is expected based on standard elasticity models (Bacon et al., 1973) where the screw line tension is much larger than that of the edge. However, for precipitates at the nanoscale, the CRSS is controlled mainly by the core energy contribution to the line tension, which is only slightly larger for the screw than for the edge (Hu et al., 2019). Thus, the typical conclusion drawn from standard models can be misleading when applied to nanoscale precipitate structures. Also, as shown below, the typical precipitate edge–edge spacing at the CRSS is also slightly larger for the screw as compared to the edge, further reducing the differences in strength.

Table 3
Simulated CRSS values for various microstructures and volume fractions f as indicated. The first three rows are simulated using 4 different glide planes in each of 2 different $3\times3\times3$ pseudo-random microstructures while the last 4 rows are calculated using 4 different glide planes in 1 pseudo-random microstructure.

f	Microstructure	Precipitate dimension $\mathbf{a}\times\mathbf{c}$	CRSS (MPa)			
			With misfit stress		Without misfit stress	
			Screw	Edge	Screw	Edge
0.66%	micro(100)	2 × 4	123 ± 10	109 ± 14	113 ± 13	103 ± 13
1.10%	micro(100)	3 × 3	164 ± 25	140 ± 8	158 ± 21	139 ± 7
1.60%	micro(100)	3 × 8	161 ± 22	147 ± 14	147 ± 13	120 ± 11
1.10%	micro(100)	2 × 4	–	–	151 ± 19	135 ± 16
1.10%	micro(111)	3 × 3	–	–	143 ± 10	128 ± 5
1.10%	micro(111) (large perturb)	3 × 3	–	–	165 ± 14	141 ± 9
1.10% (5 × 5 × 5)	micro(100)	3 × 3	–	–	160 ± 14	136 ± 6

Examining the effects of misfit stresses, Table 3 shows that the matrix misfit stresses have almost no effect on the averaged CRSS for both edge and screw, especially for f= 0.66% and 1.10%. Visualization of the critical configurations in typical cases for edge and screw are shown in Fig. 7 and are essentially identical with and without misfit stresses. This is consistent with the very local misfit stress fields shown in Fig. 4. For f = 1.60%, the misfit stresses increase the CRSS slightly (≈14 MPa for the screw and 27 MPa for the edge) due to the larger size and more-equiaxed shape that lead to larger misfit stresses in the matrix extending over a slightly longer range. Reversing the line direction to change the sign of the PK force due to RSS field leads to no statistically-different results. Overall, the effects of the matrix misfit stresses are small relative to the total CRSS and so are not crucial for reasonable determination of the CRSS in the typical peak-aged alloy (f = 1.10%). This also implies that a loss of such misfit (or coherency) stresses that may arise for larger precipitates in the overaged regime may not be a significant contribution to any decrease in strength for Orowan looping.

With costly-to-compute misfit stresses of little importance, we now focus on results computed without misfit stress in Table 3 and examine the role of geometry. The strength increases significantly from f = 0.66% to 1.10% but decreases upon a further increase in f to 1.60%. The latter effect is unexpected in traditional models. However, as known from classic analyses of Orowan strengthening (Bacon et al., 1973), the CRSS should scale as $\tau_c \propto 1/L$ where L is the edge-to-edge spacing of precipitates. We have performed a Voronoi tesselation of our microstructures to extract the average center-to-center precipitate spacing $\bar{L}$ in the entire microstructure and the average edge-to-edge precipitate spacing L along the actual dislocation at the CRSS. We also measure the edge-to-edge distance D across the precipitates pinning the dislocation at the CRSS. Examples of these geometric measurements are shown in Fig. 8. The microstructure with f = 1.10% has the smallest L while the microstructures with f = 0.66% and f = 1.60% have larger and comparable L. This is due to the fact that the f = 1.60% microstructure consists of precipitates with a larger area and shorter length, as compared to f = 1.10%. The strength is controlled by L. Analysis shows that, across all microstructures, the dislocation is pinned in a configuration that has a $L < \bar{L}$ with, typically, $L = (0.79 \pm 0.18)\bar{L}$ (screw) and $L = (0.67 \pm 0.08)\bar{L}$ (edge). The strength of the f = 1.10% microstructure is thus higher than that of both f = 0.66% and f = 1.60% mainly because it has a smaller L. The difference in strength between f = 0.66% and f = 1.60% is then mainly due to the (smaller) effect of the precipitate size D at comparable L. These results demonstrate that volume fraction is not an appropriate measure for estimating strength. The size and shape of the precipitates, and the effects of that geometry on the precipitate microstructure on the relevant dislocation glide planes, are the main microstructural determinants of the strength.

The emergence of an operative edge-to-edge spacing $L = (0.73 \pm 0.15)\bar{L}$ (average of screw and edge) across many simulations is interesting, but as yet not quantitatively explained. It seems, however, natural that the dislocation will be pinned in the strongest possible configurations, corresponding to some $L < \bar{L}$. This finding is in contradiction to the analysis of Friedel (1967) for weak point-pinning obstacles, invoked also in the BKS theory (Bacon et al., 1973). Friedel found that the dislocation will find paths with *longer* average segments ($L > \bar{L}$) in a random microstructure. However, this result in the weak-pinning limit does not apply for Orowan looping.

5.2. Role of microstructure

Here we examine the CRSS for Orowan looping across a wider range of microstructures. Due to the high cost of computing the misfit stresses, their minimal effect on the CRSS, and our interest in comparisons among structures, we consider only systems with zero misfit stresses and focus on f = 1.10%.

To assess any size dependence of our finite-size simulations, we simulated Orowan looping in a larger $5\times5\times5$ pseudo-random micro(100) microstructure (see Table 3). The CRSS is statistically identical to the results for the $3\times3\times3$ microstructure. This, as well as the small sample-to-sample strength variations among the $3\times3\times3$ microstructures, indicates that this size is sufficiently representative. The slow convergence with increasing size found for weak point-pinning obstacles (Nogaret and Rodney, 2006) does not apply to the present strong-obstacle problem.

We next compare results using the equiaxed diamond-like $2\mathbf{a}\times4\mathbf{c}$ cross-section to the previous rectangle-like $3\mathbf{a}\times3\mathbf{c}$ cross-section. Results in Table 3 show that the difference is minimal, verifying that the effect of the average precipitate cross-section size is small. The microstructures have the same average spacing $\bar{L}$ and, more importantly, the same average critical edge-to-edge spacing L at the CRSS that is the main feature controlling strength.

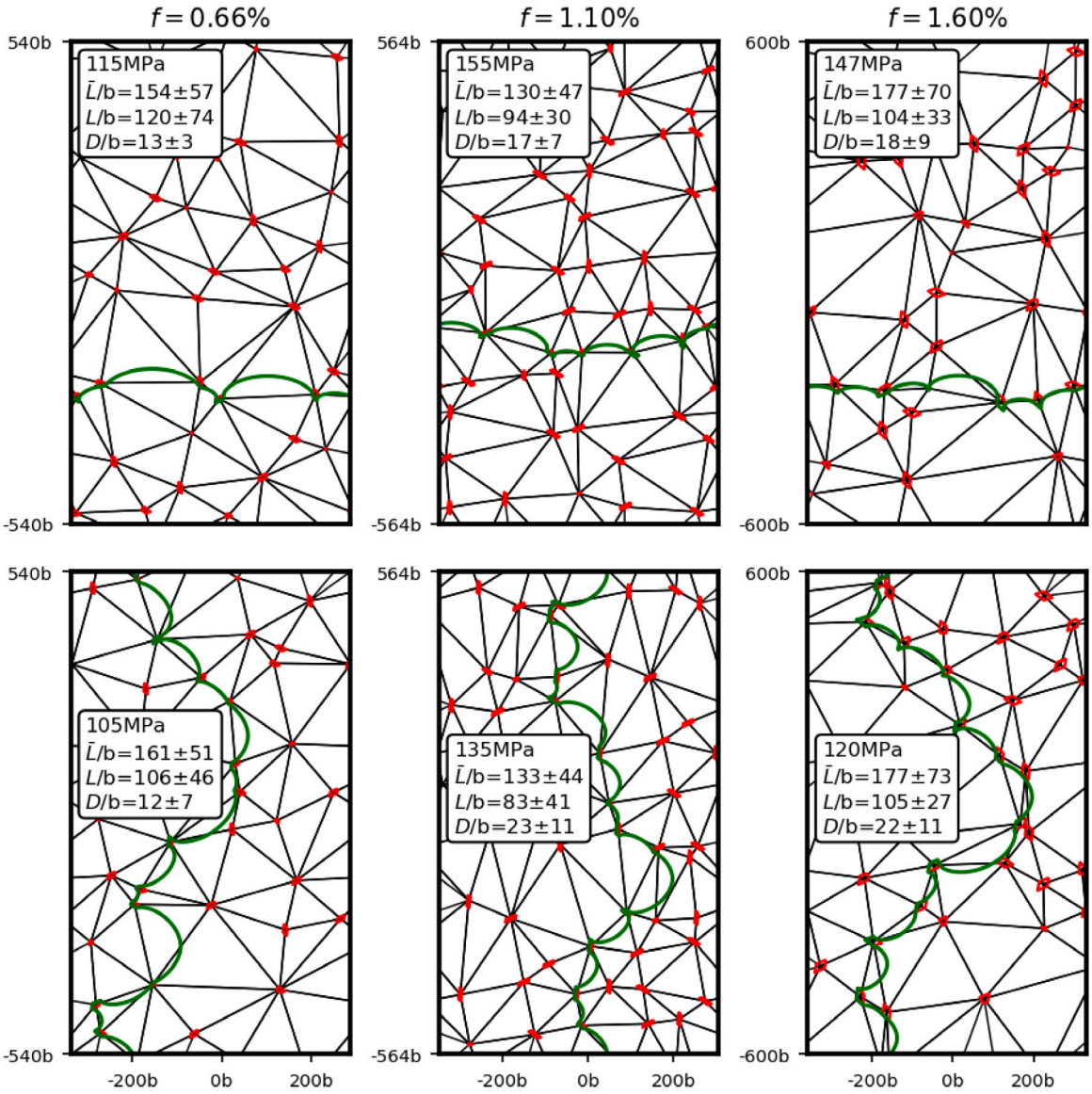

Fig. 8. Dual lattice of the Voronoi tesselation of three typical microstructures at f = 0.66%, 1.10%, and 1.60%, with the average center-to-center precipitate spacing $\bar{L}$ and average edge-to-edge precipitate distance L at the CRSS indicated. The dislocation configuration at the simulated CRSS is shown by the green line for screw (upper) and edge (lower) simulations.

Turning to the micro(111) microstructures, the CRSS for the case where precipitates do not extend outside the building block shows strengths very slightly lower than the micro(100) (see Table 3). The dislocation configuration at the CRSS for a typical case is shown in Fig. 9 along with the Voronoi tesselation. For this geometry, we find $\bar{L} = 125b$ and $L = 89b$, the latter just slightly larger than for the micro(100) cases and hence consistent with a slightly smaller CRSS. With larger perturbations enabling precipitates to cross building block boundaries, and thus partially eliminating precipitate-free channels, the CRSS is statistically identical to that for micro(100) (see Table 3). The dislocation configuration at the CRSS for a typical case is shown in Fig. 9. For this geometry, the $\bar{L}$ and L are $128b$ and $84b$, essentially identical to those found for micro(100), rationalizing the similar strengths.

Finally, we also created several random microstructures in which precipitate cross-sectional shapes were placed randomly, but without overlaps, within the domain at area fraction $f = 1.10\%$. We do not believe the purely random microstructure is appropriate for these materials, but a comparison remains interesting. The CRSS for Orowan looping in these random microstructures are statistically identical to those obtained for our pseudo-random microstructures.

From all of these studies, we conclude that the simulated CRSS for Orowan looping is quite robust across variations in the microstructure. The CRSS is thus controlled by a combination of precipitate size, shape, and volume fraction that determines $\bar{L}$

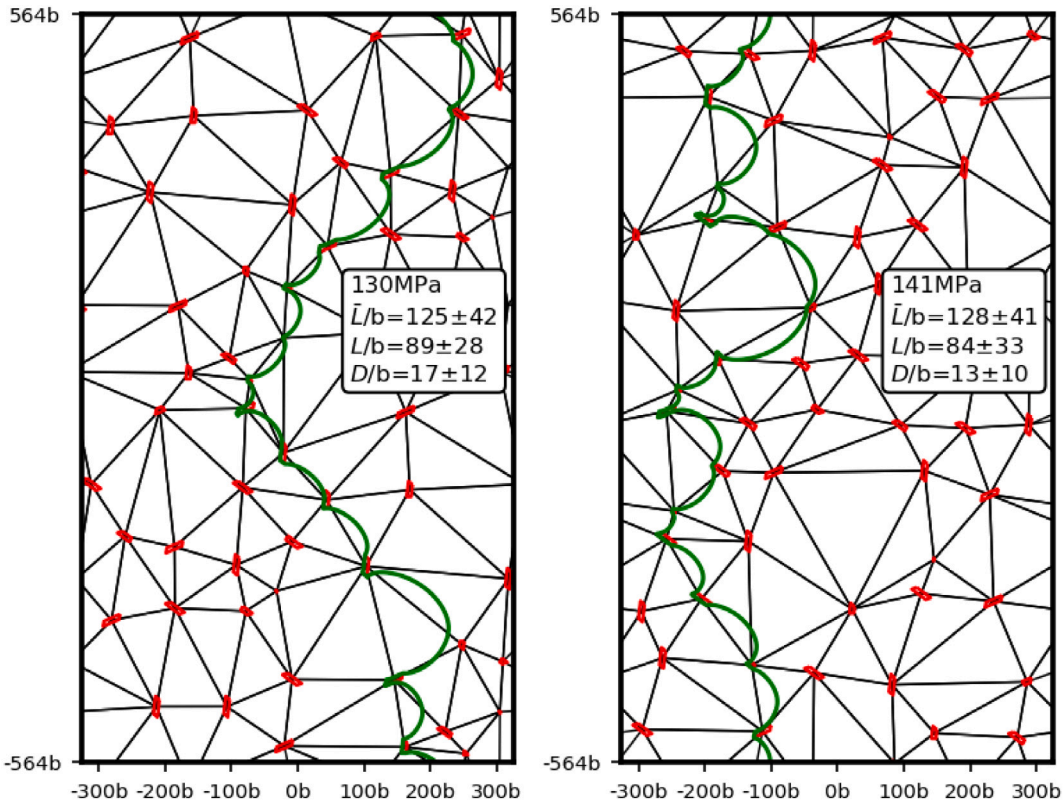

Fig. 9. Dual lattice of the Voronoi tesselation of typical micro(111) structures at $f = 1.10\%$ without (left) and with (right) large perturbations. The average center-to-center precipitate spacing $\bar{L}$ and average edge-to-edge precipitate distance L at the CRSS for an edge dislocation are shown. The dislocation configuration at the simulated CRSS is shown by the green line.

and L, with minimal secondary effects of (i) D and (ii) larger-scale differences between micro(100) and micro(111). The relative insensitivity to these microstructural aspects is important for enabling comparisons with experiment below.

5.3. Role of dislocation core energy

The classic BKS analysis of Orowan looping was based on an elasticity analysis, imposing an arbitrary cut-off length r_0 in the calculation of self-energies (Bacon et al., 1973). The total dislocation energy was then implicitly embedded in the choice of r_0 but its effects were not directly investigated. In `ParaDiS` and other DDD codes, the inelastic contributions to the total dislocation energy are either neglected or introduced as an additional core energy in an ad-hoc manner, and again the effects of the choice of this core energy on phenomena are rarely examined. Here, we demonstrate the role of a chosen core energy on the CRSS for Orowan looping and, moreover, the importance of retaining an accurate (i.e. atomistic) total dislocation energy for the nanoscale strengthening in Al-6xxx.

Specifically, in addition to the Ercolessi-Adams atomistic energy, we study several other core energy choices. Atomistically, we consider the core energy derived from the Mishin EAM potential (Mishin et al., 1999) at T = 0 K (Hu et al., 2019) and, using an entirely different analysis, at T = 300 K by Geslin and Rodney (2018) who found $a = 1.2b$ as optimal in calibrating to `ParaDiS`. We then also consider the `ParaDiS` default core model $E_c(\theta) = \frac{\mu b^2}{4\pi}\ln(\frac{a}{0.1b})(\cos^2\theta + \frac{1}{1-\nu}\sin^2\theta)$, while noting that there is an additional contribution to the total energy in the non-singular theory that is also automatically included (Hu et al., 2019). Finally, we examine a hybrid model as follows. We use the Ercolessi–Adams atomistic core energy measured at $a = 5.4b$ but then compute all segment–segment elastic interactions in `ParaDiS` using a much lower shear modulus $\mu = 10$ GPa. This hybrid model thus suppresses the effects of long-range elastic interactions beyond $a = 5.4b$. The material parameters for all of these test cases are shown in Table 4. The screw and edge core energies are all quoted at the common value of $a = b$ for comparison purposes. The full character-dependent core energies $E_c(\theta)$ that dictate the core contributions to the dislocation line tension $\Gamma_c = E_c(\theta) + \partial^2 E_c(\theta)/\partial\theta^2$ are used in the DDD simulations. DDD results that preserve the total atomistic energy are essentially independent of a. For instance, we have verified, using simple periodic geometries, that using the Ercolessi-Adams potential at T = 0 K calibrated with $a = 1.2b$ gives results identical to those calibrated at $a = 5.4b$.

Results for the CRSS of the $f = 1.10\%$ micro(100) case averaged over 4 different glide planes are shown in Table 4 for the different core models. Use of the T = 0 K core energy from the Mishin potential yields statistically identical results to those using

Table 4
Material parameters and dislocation core energies used in parametric studies of the CRSS for Orowan looping. Shear modulus and Poisson ratio are obtained by Bacon–Scattergood effective properties. Dislocation core energies are quoted at $a = b$. The core energy for Geslin and Rodney (2018) is recovered from their line tension calibration, and the NS additional term is added back for consistent comparison (Hu et al., 2019). The value of a used in ParaDiS for each case is shown. The CRSS for the $f = 1.10\%3 \times 3 \times 3$ micro(100) structure is then shown for each case.

Core model	μ (GPa)	ν	E_c, a = b (eV/nm)		a	CRSS (MPa)	
			Screw	Edge		Screw	Edge
Ercolessi-Adams, T = 0 K (Hu et al., 2019)	32.0	0.34	0.810	0.463	5.4b	158 ± 21	139 ± 7
Mishin, T = 0 K (Hu et al., 2019)	28.7	0.35	1.262	1.198	1.2b	157 ± 24	140 ± 14
Mishin, T = 300 K (Geslin and Rodney, 2018)	28.7	0.35	0.939	0.732	1.2b	138 ± 23	124 ± 13
ParaDiS (Arsenlis et al., 2007)	32.0	0.34	2.972	4.504	1b	289 ± 26	254 ± 18
Hybrid	10.0	0.33	0.810	0.463	5.4b	135 ± 12	133 ± 8

the Ercolessi-Adams potential. The core energies for edge and screw do differ slightly (see Table 4), but Orowan looping involves the full line tension Γ and so differences between edge and screw are not sufficient for a quantitative comparison. The use of the Geslin et al. calibration to the Mishin potential at 300 K (Geslin and Rodney, 2018) leads to a modest decrease in the CRSS of 16–21 MPa. All the atomistically-calibrated results are thus quite comparable. In contrast, use of the default ParaDiS core energy model leads to a huge increase, nearly doubling the CRSS for Orowan looping while still using the Ercolessi-Adams elastic constants.

Finally, the limited role of the long-range elastic energies is demonstrated by the hybrid model (reduced-modulus simulation that retains the Ercolessi–Adams core energy at $a = 5.4b$). The CRSS for this hybrid model is reduced by only 23 MPa (15%) for the screw and only 6 MPa (5%) for the edge. Standard elasticity-based models and simulations would show that all strengths scale directly with μ. While the core energy has some interplay with μ and a, results of Hu et al. (2019) for Al, Cu, and Ni show that the core energies at a fixed a are not directly proportional to the corresponding shear moduli. Accurate modeling, relative to atomistic models, thus requires a proper calibration of a core energy contribution to the total dislocation energy versus character for a chosen scale a. Accurate results for the CRSS of Orowan looping here requires an accurate representation of the energy within $a = 5.4b$ (independent of its partitioning between elastic and core contributions), with long-range elastic interactions having a very small effect.

5.4. Comparison with experiments

In commercial Al-6061, Ozturk et al. examined both the yield strength and the hardness as a function of aging time (Ozturk et al., 2010). When the precipitate microstructure is well-formed (around peak aging), they showed that the tensile yield stress (in MPa) was quantitatively equal to 3 times the Vickers Hardness, $\sigma_y = 3$HV. This is essentially the relationship between yield and hardness derived by Taylor for an elastic/perfectly-plastic material. This relationship presumably applies well to this system because the work-hardening rate is quite low around the peak aged condition. Using this validated relationship, the measured hardness of 97 kg/mm^2 in the A2(NA+AA) alloy studied by Wenner et al. (2012) corresponds to a tensile yield stress of 291 MPa. The peak-aged strength in Al-6061 measured by Ozturk et al. but without any microstructural information, was comparable at 275 MPa. For an alloy denoted as A12 having a microstructure with $f = 1.2\%$ containing longer (69 nm) and larger-area (12.2 nm^2) precipitates, Marioara et al. (2007) report a peak-aged hardness of 104 kg/mm^{-2} corresponding to a yield stress of 312 MPa. Thus, all results on peak-aged materials are fairly similar.

The Orowan looping strengths for screw and edge dislocations in the representative $f = 1.10\%$ $3 \times 3 \times 3$ pseudo-random microstructures using the Ercolessi-Adams EAM Al T = 0 K elastic constants, core energy (Ercolessi and Adams, 1994; Hu et al., 2019), and misfit stresses are 164 MPa and 140 MPa, with an average of 152 MPa. Using a Taylor factor of 3.06 for an untextured large-grain polycrystal, we thus estimate the tensile strength as 465 MPa. We have shown that this strength is robust against a range of microstructural differences and atomistically-calibrated core energies at T = 0 K, and is much smaller than the CRSS coming from a default ParaDiS simulation. Nonetheless, this result is significantly higher (≈ 50%) than the experimental strengths of ≈300 MPa.

The experiments are at room temperature. Using the average reduction in CRSS of 17.5 MPa found when using the room temperature core energy of Geslin and Rodney (2018) for the Mishin potential (Mishin et al., 1999), the predicted strength is reduced to 411 MPa. This improves the agreement with experiment but remains roughly 33% higher than experiments. Thermal activation of precipitate strengthening at finite T and experimental strain rates is usually quite small, as revealed by standard Haasen plots (Argon, 2008), and so is unlikely to explain this remaining difference.

Overall, we conclude that the modeling of Orowan looping using realistic precipitate microstructures, state-of-the-art computational methods, and atomistically-calibrated dislocation core energies, results in a non-negligible *over-prediction* of the room-temperature strength of peak-aged Al–Mg–Si alloys. Our findings indicate that, while Orowan looping may provide an upper bound for the yield stress, the yield stress at peak aging is not quantitatively determined by Orowan looping. This finding is in contrast to standard metallurgical wisdom. However, it is only by the full quantitative study here that such a conclusion can be made.

6. Precipitate shearing

In the previous sections, we have modeled Orowan looping with what we believe is the highest degree of realism at above-atomistic scales. We have not included dislocation dissociation into two partial dislocations separated by a stacking fault ribbon nor

elastic mismatch effects, both of which are computationally demanding and not likely to bridge the gap between experiments and simulations. As a result, we deduce that precipitate shearing is most likely occurring and is the controlling mechanism even at peak aging. This deduction is actually consistent with very recent experimental TEM observations of multiply-sheared precipitates in this alloy (Christiansen et al., 2019), but is not consistent with the traditional textbook view of the strengthening at peak aging. Here, we therefore make a preliminary examination of precipitate shearing.

The critical material parameter for precipitate shearing is the generalized fault energy corresponding to shearing of the precipitate by Al [110]a/2-type dislocations gliding on (111)-type planes. This information has heretofore been unknown, making assessment of shearing impossible in this alloy. These generalized fault energies were recently computed, however, for the three β'' precipitates using first-principles Density-Functional Theory (Jain et al., 2021). Across all the [110]a/2 Al Burgers vectors projected onto the $(51\bar{1})$ and (112) planes in β'' that align nearly perfectly with the Al (111) slip planes, a typical accessible shearing fault energy can be estimated as $\gamma_f = 450$ mJ/m^2.

We first consider the shearing in terms of forces. For a dislocation shearing into a rectangular precipitate along an edge of length D, the force required to overcome the fault energy is $F = \gamma_f D$. For the precipitates here with typical precipitate dimension $D = \sqrt{A} = 3$ nm and $\gamma_f = 450$ mJ/m^2, the typical necessary force is $F = 1.35$ nN. Fig. 10 shows the total forces acting on the precipitates at the critical stress for Orowan looping as computed by DDD. The individual nodal forces are concentrated at the precipitate corners (not shown), with the forces along the straight pinned regions comparatively small. This is expected since these (configurational) forces are dominated by the core energy and line tension concentrated in regions of high curvature or high angle change. The total force exceeds the estimated shearing force of $F = 1.35$ nN in 10 of 17 precipitates for the edge and 4 of 12 precipitates for the screw. Thus, the DDD results indicate that significant precipitate shearing could occur prior to Orowan looping. However, the forces acting on the precipitates do not significantly exceed the shearing force, and so the onset of shearing using this estimate would occur at stresses only somewhat lower than the Orowan stresses.

The above analysis does not include the effects of the misfit stresses inside the precipitate. We thus now examine an overall energy balance for the shearing of an average precipitate that accounts for the applied stress, the internal precipitate misfit stress, and the shearing energy cost as follows. For simplicity, we consider the cutting of a square $D \times D$ precipitate parallel to the edge of the precipitate. A single precipitate is cut with the dislocation pinned at the neighboring precipitates as shown schematically in Fig. 11. An analysis of cutting diagonally starting at the apex of the square leads to a more-complex result where thermal activation must be considered but final quantitative results at experimental temperatures and strain rates are quite similar to those of the analysis we show now.

As shown in Fig. 11, when the dislocation cuts the precipitate over an incremental distance $\mathrm{d}x$ the two adjacent dislocation segments of length L_s in the matrix bowout such that the applied stress τ does work on the system of $\tau b L_s \,\mathrm{d}x$. Work of $\tau_{\text{misfit}} bD \,\mathrm{d}x$ is also done by the *internal* precipitate misfit stress τ_{misfit}. We consider those precipitates where the sign of the misfit stress assists the cutting. Finally, the energetic cost of creating the additional area of faulted precipitate is $\gamma_f D \,\mathrm{d}x$. Precipitate shearing is achieved at the stress for which the net incremental energy cost is zero, $\tau b L_s \,\mathrm{d}x + \tau_{\text{misfit}} bD \,\mathrm{d}x - \gamma_f D \,\mathrm{d}x = 0$. This leads to the critical stress (strength for precipitate shearing) of

$$\tau_{\text{c}} = \frac{\gamma_f D - \tau_{\text{misfit}} bD}{bL_s} \tag{4}$$

In appropriately-oriented precipitates, the internal precipitate misfit stress can act as an effective reduction of the fault energy, lowering the strength for shearing. Once these precipitates shear and the dislocation advances, the remaining precipitates will either shear or be by-passed by Orowan looping at this stress; this will be examined by DDD below.

We apply the above analysis using values for alloy A2(NA+AA) of $D = 3$ nm, precipitate center-to-center distance $\bar{L} = \sqrt{6} l_{\text{c}}/3 = 35.8$ nm, and hence $L_s = \bar{L} - D$, $b = 2.851$ Å, and $\gamma_f = 450$ mJ/m^2. The sign of the misfit RSS depends on Burgers vector and line direction, and so only some of the precipitates will assist shearing but the absolute magnitude of the shearing is clear, with an average of 347 MPa for screw dislocations and 266 MPa edge dislocations. The predicted CRSS values for shearing are 113 MPa for the screw and 120 MPa for the edge. Taking the average of 116.5 MPa corresponds to a tensile yield stress of $\sigma_y = 356$ MPa, which is much closer to experiments. Local statistical fluctuations or a reduction of the GSFE energies with temperature (Warner and Curtin, 2009) would reduce the CRSS, while dislocation pinning at smaller values of L_s would increase the CRSS; these are beyond the scope of the present analysis.

We can then use DDD to verify that the CRSS due to shearing of favorable precipitates would allow subsequent Orowan looping and/or shearing of any remaining precipitates. This is done by approximately mimicking the consequences of precipitate shearing as follows. We perform a DDD simulation in which all precipitates that would be cut with the assistance of the internal precipitate misfit stresses are removed at the start of the simulation. This leaves a microstructure with 1/3 fewer precipitates for the edge and 2/3 fewer precipitates for the screw. In such a modified $f = 1.10\%$ micro(100) microstructure, the average CRSS values for the residual Orowan looping are 105 MPa and 103 MPa for screw and edge dislocations. These reductions are consistent with larger precipitate spacing $\bar{L}$ due to fewer precipitates, and we find the corresponding critical L values to have a ratio $L/\bar{L}$ similar to those in the original microstructures. Most importantly, these values for looping are lower than the estimated CRSS values for the initial shearing so that the initial shearing that would control the CRSS. Finally, at the CRSS for looping in these modified microstructures, the forces acting on the unsheared precipitates are shown in Fig. 12 and some of them can again exceed the shearing resistance $\gamma_f D + |\tau_{\text{misfit}}| bD$ even though the remaining misfit stresses now inhibit shearing. Thus, after shearing of the initial shearable precipitates, both shearing and looping are estimated to enable dislocation motion through the remainder of the precipitates in the microstructure.

Overall, this preliminary theoretical and simulation study of shearing indicates that the CRSS in peak-aged Al-6xxx should be controlled by precipitate shearing rather than Orowan looping, and that the estimated CRSS values are closer to experimental strengths.

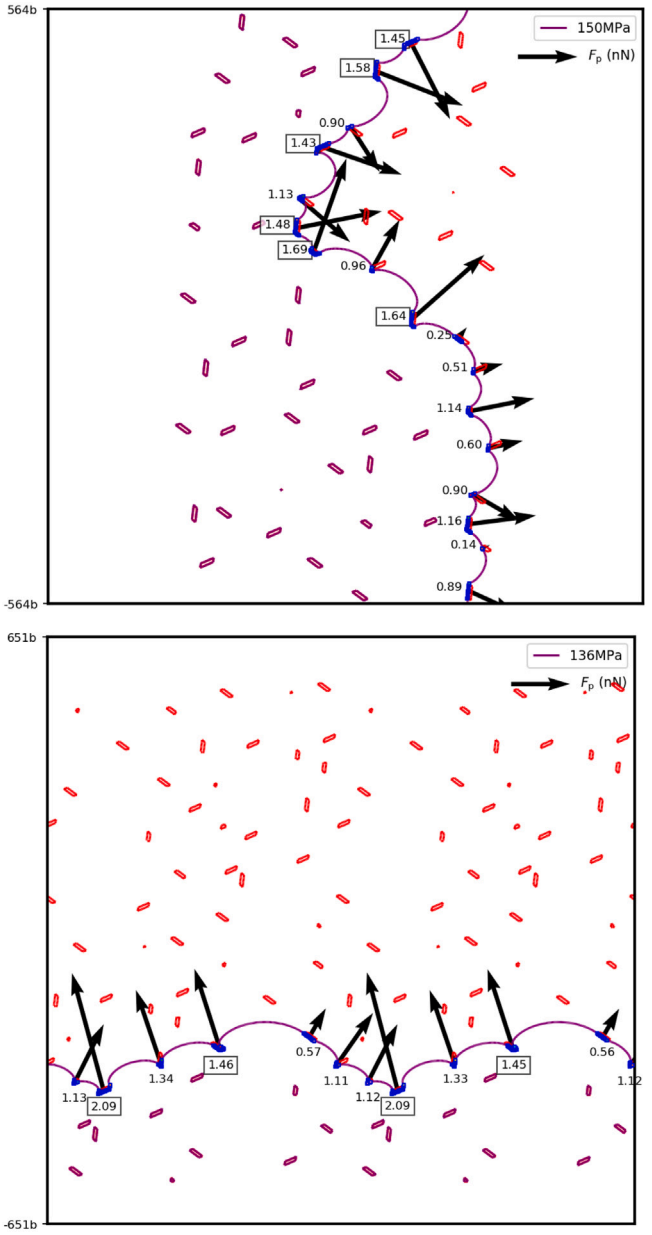

Fig. 10. Forces F_p exerted by the dislocation on each precipitate as computed in DDD, for edge (top) and screw (bottom) dislocations at the CRSS for Orowan looping. These forces are to be compared with the critical value for shearing of $\gamma_f D$ =1.35 nN, with values shown in boxes exceeding this value.

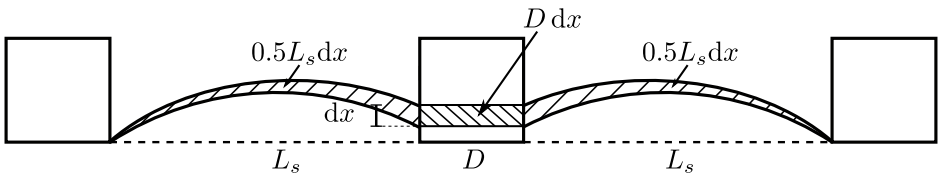

Fig. 11. Shearing of a precipitate by a dislocation, showing the incremental areas swept by the dislocation for an advance by distance dx inside the precipitate.

7. Conclusions

We have presented a detailed analysis of dislocation motion through realistic precipitate microstructures in Al-6xxx (Al–Mg–Si) alloys at the peak-aging condition with the goal of making quantitative connection with experiments.

We first examined Orowan looping as the controlling strengthening mechanism, since Orowan looping and precipitate shearing are believe to give the same strength at peak-aging. We created realistic pseudo-random precipitate microstructures, calculated the misfit stress fields, and examined dislocation motion using Discrete Dislocation Dynamics. We found that (i) matrix misfit stresses have little influence on the CRSS for looping, (ii) the CRSS for screw and edge are quite similar, in contrast to classic elasticity models (Bacon et al., 1973), (iii) the CRSS is controlled by a critical edge-to-edge precipitate spacing L that is smaller than the average spacing $\bar{L}$ with $L/\bar{L} \approx 0.73$, in contrast to the weak-pinning Friedel model, with other microstructural features of less importance, and (iv) dislocation core energies dominate over longer-range elastic energies so that calibrated atomistic core energies are essential for quantitative results. All of these findings are new. With a room temperature atomistic core energy, we predict a tensile yield strength that remains 33% above the experimental value. The Orowan looping mechanism is thus only an approximate upper bound for the tensile yield strength in this peak-aged alloy.

Analysis of the DDD-computed forces on precipitates and the resisting forces derived from precipitate generalized stacking fault energy shows that many precipitates could be sheared prior to Orowan looping. An energy-based prediction of precipitate shearing that includes the effects of the internal precipitate misfit stresses then leads to an estimated CRSS that is closer to experiments. We see two paths for future research to examine shearing. The first path remains at the DDD level but follows shearing processes precipitate-by-precipitate. The second path is atomistic simulations in simple periodic microstructures to extract critical conditions for shearing; this path is becoming feasible due to the emergence of new machine-learning interatomic potentials for Al–Mg–Si (Jain et al., 2021).

Overall, this study demonstrates a number of new findings that indicate that classical and continuum analyses quantitatively fail when applied to nanoscale microstructures such as peak-aged Al-6xxx. Accurate modeling requires detailed microstructures, calibrated dislocation energies, relevant misfit stresses, and realistic precipitate shearing energies. Fortunately, all of these new aspects are computationally accessible, so that the general methodology introduced here can be widely applied to Al and other alloys that rely on nanoscale precipitation to achieve strengths that make them technologically valuable. The present approach can further be used to understand how strength can be optimized by modifications to microstructure or chemistry of precipitates, thus providing guidance to future alloy development.

CRediT authorship contribution statement

Yi Hu: Methodology, Formal analysis, Investigation, Writing. **W.A. Curtin:** Conceptualization, Methodology, Formal analysis, Supervision, Writing.

Declaration of competing interest

The authors declare that they have no known competing financial interests or personal relationships that could have appeared to influence the work reported in this paper.

Acknowledgments

The authors acknowledge support for this work by the NCCR MARVEL, funded by the Swiss National Science Foundation. The authors also thank D. Marchand for providing the DFT β'' fault energies and Dr. T. Junge for his help in FFT calculation.

Appendix. Introduction of FFT method

For the elastic misfit stress calculations, we use a variational FFT-based method to approximate the solution to the equilibrium equations on a regular periodic pixel or voxel grid (Zeman et al., 2017) as in the open source package μ Spectre (Junge et al., 2020).

The basic idea of the method is to use the discrete Fourier transform basis functions $\varphi_{\mathbf{q}_m}(\mathbf{x})$ as shape functions for a Galerkin discretization of the periodic domain,

$$\varphi_{\mathbf{q}_m}(\mathbf{x}) = \exp\left(2\pi\, i \mathbf{q}_m \cdot \mathbf{x}\right), \tag{A.1}$$

where $\mathbf{q}_m$ is the normalized wave vector of the mth Fourier space grid point. These basis functions are interpolatory and constitute a partition of unity.

Standard Galerkin discretization then allows for a determination of the stiffness matrix $\mathbf{C}$ of the discretized problem and for the solution of the linear elasticity problem as

$$\mathbf{Cu} = -\mathbf{Cu}_{\text{ref}}, \tag{A.2}$$

where $\mathbf{u}$ is the vector of nodal displacements and $\mathbf{u}_{\text{ref}}$ is a uniform displacement due to applied strain boundary conditions. One can also express the stiffness matrix $\mathbf{C}_{\text{ref}}$ of a replacement problem with the same discretization grid, but uniform material properties. This reference stiffness matrix $\mathbf{C}_{\text{ref}}$ corresponds a convolution and can therefore be expressed *and inverted* in Fourier space at low

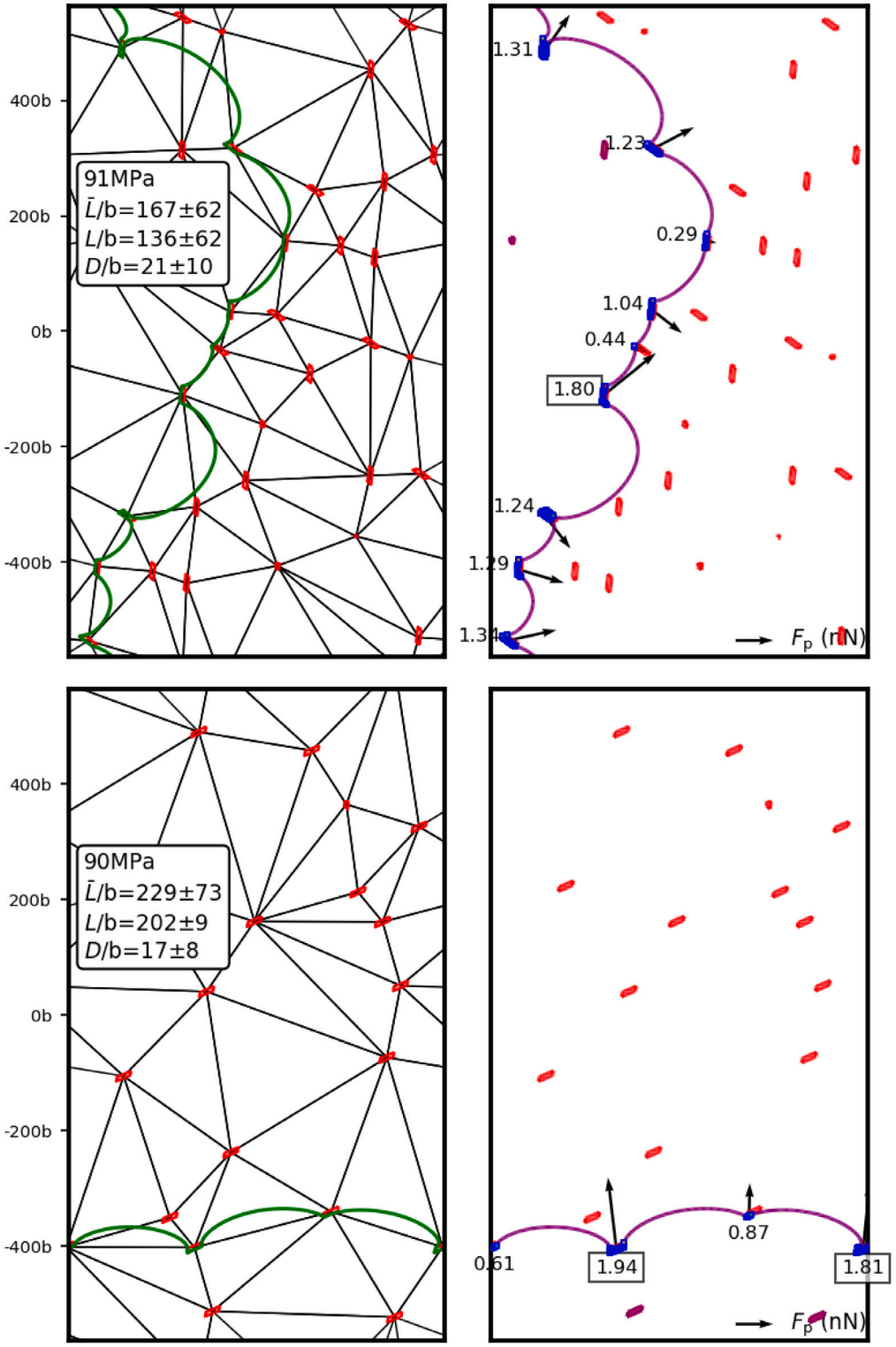

Fig. 12. DDD simulations of dislocation motion through microstructures where the shearable precipitates have been removed, for edge (above) and screw (below) cases. Left figures show the critical configuration and relevant spacings. Right figures show the forces acting on the precipitates at the critical configuration, with boxed values above the critical resisting force $\gamma_f D + |\tau_{\text{misfit}}|bD$ (1.65 nN for edge and 1.58 nN for screw, respectively).

computational cost. The inverse $\mathbf{\Gamma} = \mathbf{C}_{\text{ref}}^{-1}$ corresponds to the discretized Greens function of the problem and happens to be a preconditioner to the problem (A.2) with excellent spectral properties.

The preconditioned problem

$$\mathbf{\Gamma C u} = -\mathbf{\Gamma C u}_{\text{ref}}, \tag{A.3}$$

can be solved very efficiently using projection-based solvers such as the conjugate gradient method.

Note that the formulation in Zeman et al. (2017) makes a modification to the stiffness matrix such that the unknowns are strains $\boldsymbol{\epsilon}$ instead of $\mathbf{u}$, leading to the main equation

$$\mathbf{GK}\boldsymbol{\epsilon} = -\mathbf{G}\boldsymbol{\sigma}, \tag{A.4}$$

where $\mathbf{G}$ and $\mathbf{K}$ correspond to the modified Greens function matrix $\mathbf{\Gamma}$ and the modified stiffness matrix $\mathbf{C}$, and $\boldsymbol{\sigma}$ corresponds Cauchy stress. The modifications are straight-forward and omitted here for brevity. The interested reader will find them well explained in Zeman et al. (2017).

References

Aagesen, L.K., Miao, J., Allison, J.E., Aubry, S., Arsenlis, A., 2018. Prediction of Precipitation Strengthening in the Commercial Mg Alloy AZ91 using dislocation dynamics. Metall. Mater. Trans. A 49 (5), 1908–1915. http://dx.doi.org/10.1007/s11661-018-4530-6.

Andersen, S.J., Marioara, C.D., Friis, J., Wenner, S., Holmestad, R., 2018. Precipitates in aluminium alloys. Adv. Phys. X 3 (1), 1479984. http://dx.doi.org/10.1080/23746149.2018.1479984.

Andersen, S.J., Zandbergen, H.W., Jansen, J., TrÆholt, C., Tundal, U., Reiso, O., 1998. The crystal structure of the B'' phase in Al–Mg–Si alloys. Acta Mater. 46 (9), 3283–3298. http://dx.doi.org/10.1016/S1359-6454(97)00493-X.

Argon, A.S., 2008. Strengthening Mechanisms in Crystal Plasticity. In: Oxford Series on Materials Modelling, number 4, Oxford University Press, Oxford ; New York.

Arsenlis, A., Cai, W., Tang, M., Rhee, M., Oppelstrup, T., Hommes, G., Pierce, T.G., Bulatov, V.V., 2007. Enabling strain hardening simulations with dislocation dynamics. Modelling Simulation Mater. Sci. Eng. 15 (6), 553. http://dx.doi.org/10.1088/0965-0393/15/6/001.

Bacon, D.J., Kocks, U.F., Scattergood, R.O., 1973. The effect of dislocation self-interaction on the orowan stress. Phil. Mag. 28 (6), 1241–1263. http://dx.doi.org/10.1080/14786437308227997.

Bardel, D., Perez, M., Nelias, D., Deschamps, A., Hutchinson, C.R., Maisonnette, D., Chaise, T., Garnier, J., Bourlier, F., 2014. Coupled precipitation and yield strength modelling for non-isothermal treatments of a 6061 aluminium alloy. Acta Mater. 62, 129–140. http://dx.doi.org/10.1016/j.actamat.2013.09.041.

Cai, W., Arsenlis, A., Weinberger, C.R., Bulatov, V.V., 2006. A non-singular continuum theory of dislocations. J. Mech. Phys. Solids 54 (3), 561–587. http://dx.doi.org/10.1016/j.jmps.2005.09.005.

Christiansen, E., Marioara, C.D., Holmedal, B., Hopperstad, O.S., Holmestad, R., 2019. Nano-scale characterisation of sheared β'' precipitates in a deformed Al-Mg-Si alloy. Sci. Rep. 9 (1), 1–11. http://dx.doi.org/10.1038/s41598-019-53772-4.

Ercolessi, F., Adams, J.B., 1994. Interatomic potentials from first-principles calculations: the force-matching method. Europhys. Lett. 26 (8), 583. http://dx.doi.org/10.1209/0295-5075/26/8/005.

Esteban-Manzanares, G., Ma, A., Papadimitriou, I., Martínez, E., LLorca, J., 2019. Basal dislocation/precipitate interactions in Mg–Al alloys: An atomistic investigation. Modelling Simulation Mater. Sci. Eng. 27 (7), 075003. http://dx.doi.org/10.1088/1361-651X/ab2de0.

Fivel, M.C., 2008. Discrete dislocation dynamics: An important recent break-through in the modelling of dislocation collective behaviour. C. R. Phys. 9 (3), 427–436. http://dx.doi.org/10.1016/j.crhy.2007.11.005.

Friedel, J., 1967. Dislocations. Pergamon Press.

Geslin, P.-A., Rodney, D., 2018. Thermal fluctuations of dislocations reveal the interplay between their core energy and long-range elasticity. Phys. Rev. B 98 (17), 174115. http://dx.doi.org/10.1103/PhysRevB.98.174115.

Giofré, D., Junge, T., Curtin, W.A., Ceriotti, M., 2017. Ab initio modelling of the early stages of precipitation in Al-6000 alloys. Acta Mater. 140 (Supplement C), 240–249. http://dx.doi.org/10.1016/j.actamat.2017.08.017.

Hirth, J.P., Lothe, J., 1982. Theory of Dislocations. Krieger Publishing Company.

Hu, Y., Szajewski, B.A., Rodney, D., Curtin, W.A., 2019. Atomistic dislocation core energies and calibration of non-singular discrete dislocation dynamics. Modelling Simulation Mater. Sci. Eng. 28 (1), 015005. http://dx.doi.org/10.1088/1361-651X/ab5489.

Jain, A., Glensk, A., Marchand, D., Mak, E., Curtin, W.A., 2021. Machine learning for Metallurgy II. A Neural Network Potential for Al-Mg-Si. in preparation.

Junge, T., Ali, F., Richart, N., Pastewka, L., Leute, R., Zeman, J., Doškář, M., Ladecký, M., Pultarova, I., 2020. μSPectre, open-source platform for efficient FFT-based continuum mesoscale modelling. https://gitlab.com/muspectre/muspectre.

Kobayashi, R., Giofré, D., Junge, T., Ceriotti, M., Curtin, W.A., 2017. Neural network potential for Al-Mg-Si alloys. Phys. Rev. Mater. 1 (5), http://dx.doi.org/10.1103/PhysRevMaterials.1.053604.

Lehtinen, A., Granberg, F., Laurson, L., Nordlund, K., Alava, M.J., 2016. Multiscale modeling of dislocation-precipitate interactions in Fe: from molecular dynamics to discrete dislocations. Phys. Rev. E 93 (1), 013309. http://dx.doi.org/10.1103/PhysRevE.93.013309.

Maisonnette, D., Suery, M., Nelias, D., Chaudet, P., Epicier, T., 2011. Effects of heat treatments on the microstructure and mechanical properties of a 6061 aluminium alloy. Mater. Sci. Eng. A 528 (6), 2718–2724. http://dx.doi.org/10.1016/j.msea.2010.12.011.

Marioara, C.D., Andersen, S.J., Stene, T.N., Hasting, H., Walmsley, J., Helvoort, A.T.J.V., Holmestad, R., 2007. The effect of Cu on precipitation in Al–Mg–Si alloys. Phil. Mag. 87 (23), 3385–3413. http://dx.doi.org/10.1080/14786430701287377.

Marioara, C.D., Andersen, S.J., Zandbergen, H.W., Holmestad, R., 2005. The influence of alloy composition on precipitates of the Al-Mg-Si system. Metall. Mater. Trans. A 36 (3), 691–702. http://dx.doi.org/10.1007/s11661-005-0185-1.

Marioara, C.D., Nordmark, H., Andersen, S.J., Holmestad, R., 2006. Post-B'' phases and their influence on microstructure and hardness in 6xxx Al-Mg-Si alloys. J. Mater. Sci. 41 (2), 471–478. http://dx.doi.org/10.1007/s10853-005-2470-1.

Mishin, Y., Farkas, D., Mehl, M.J., Papaconstantopoulos, D.A., 1999. Interatomic potentials for monoatomic metals from experimental data and ab initio calculations. Phys. Rev. B 59 (5), 3393–3407. http://dx.doi.org/10.1103/PhysRevB.59.3393.

Mohles, V., Nembach, E., 2001. The Peak- and overaged states of particle strengthened materials: Computer simulations. Acta Mater. 49 (13), 2405–2417. http://dx.doi.org/10.1016/S1359-6454(01)00153-7.

Monnet, G., Naamane, S., Devincre, B., 2011. Orowan strengthening at low temperatures in bcc materials studied by dislocation dynamics simulations. Acta Mater. 59 (2), 451–461. http://dx.doi.org/10.1016/j.actamat.2010.09.039.

Myhr, O.R., Hopperstad, O.S., Børvik, T., 2018. A combined precipitation, yield stress, and work hardening model for Al-Mg-Si Alloys Incorporating the effects of strain rate and temperature. Metall. Mater. Trans. A 49 (8), 3592–3609. http://dx.doi.org/10.1007/s11661-018-4675-3.

Nembach, E., 1997. Particle Strengthening of Metals and Alloys. Wiley, New York.
Nie, J.-F., 2014. 20 - physical metallurgy of light alloys. In: Laughlin, D.E., Hono, K. (Eds.), Physical Metallurgy (Fifth Edition). Elsevier, Oxford, pp. 2009–2156. http://dx.doi.org/10.1016/B978-0-444-53770-6.00020-4.
Ninive, P.H., Løvvik, O.M., Strandlie, A., 2014. Density Functional Study of the B'' Phase in Al-Mg-Si Alloys. Metall. Mater. Trans. A 45 (6), 2916–2924. http://dx.doi.org/10.1007/s11661-014-2214-4.
Nogaret, T., Rodney, D., 2006. Finite-size effects in dislocation glide through random arrays of obstacles: Line tension simulations. Phys. Rev. B 74 (13), 134110. http://dx.doi.org/10.1103/PhysRevB.74.134110.
Ozturk, F., Sisman, A., Toros, S., Kilic, S., Picu, R.C., 2010. Influence of aging treatment on mechanical properties of 6061 aluminum alloy. Mater. Des. 31 (2), 972–975. http://dx.doi.org/10.1016/j.matdes.2009.08.017.
Queyreau, S., Devincre, B., 2009. Bauschinger effect in precipitation-strengthened materials: A dislocation dynamics investigation. Phil. Mag. Lett. 89 (7), 419–430. http://dx.doi.org/10.1080/09500830903005433.
Santos-Güemes, R., Bellón, B., Esteban-Manzanares, G., Segurado, J., Capolungo, L., LLorca, J., 2020. Multiscale modelling of precipitation hardening in Al–Cu alloys: Dislocation dynamics simulations and experimental validation. Acta Mater. 188, 475–485. http://dx.doi.org/10.1016/j.actamat.2020.02.019.
Santos-Güemes, R., Esteban-Manzanares, G., Papadimitriou, I., Segurado, J., Capolungo, L., LLorca, J., 2018. Discrete dislocation dynamics simulations of dislocation-Θ' precipitate interaction in Al-Cu alloys. J. Mech. Phys. Solids 118, 228–244. http://dx.doi.org/10.1016/j.jmps.2018.05.015.
Scattergood, R.O., Bacon, D.J., 1975. The Orowan mechanism in anisotropic crystals. Phil. Mag. 31 (1), 179–198. http://dx.doi.org/10.1080/14786437508229295.
Singh, C.V., Warner, D.H., 2013. An Atomistic-based hierarchical multiscale examination of Age Hardening in an Al-Cu Alloy. Metall. Mater. Trans. A 44 (6), 2625–2644. http://dx.doi.org/10.1007/s11661-013-1614-1.
Vaid, A., Guénolé, J., Prakash, A., Korte-Kerzel, S., Bitzek, E., 2019. Atomistic simulations of basal dislocations in Mg interacting with Mg17Al12 precipitates. Materialia 7, 100355. http://dx.doi.org/10.1016/j.mtla.2019.100355.
Warner, D., Curtin, W., 2009. Origins and implications of temperature-dependent activation energy barriers for dislocation nucleation in face-centered cubic metals. Acta Mater. 57 (14), 4267–4277. http://dx.doi.org/10.1016/j.actamat.2009.05.024.
Wenner, S., Holmestad, R., 2016. Accurately measured precipitate–matrix misfit in an Al–Mg–Si alloy by electron microscopy. Scr. Mater. 118, 5–8. http://dx.doi.org/10.1016/j.scriptamat.2016.02.031.
Wenner, S., Marioara, C.D., Andersen, S.J., Holmestad, R., 2012. Effect of room temperature storage time on precipitation in Al–Mg–Si(–Cu) alloys with different Mg/Si ratios. Int. J. Mater. Res. 103 (8), 948–954. http://dx.doi.org/10.3139/146.110795.
Zeman, J., de Geus, T.W.J., Vondřejc, J., Peerlings, R.H.J., Geers, M.G.D., 2017. A finite element perspective on nonlinear FFT-based micromechanical simulations. Internat. J. Numer. Methods Engrg. 111, 903–926. http://dx.doi.org/10.1002/nme.5481, vol. 111, issue 10, pp. 903-926.